**Electronic Supplementary Information**

# $Mo^{6+}$-$P^{5+}$ co-doped $Li_2ZnTi_3O_8$ anode for Li-storage in wide temperature range and applications in $LiNi_{0.5}Mn_{1.5}O_4/Li_2ZnTi_3O_8$ full cells

Zhongxue Zhang,[a] Lianjing Feng,[a] Huanhuan Liu,[a] Lijuan Wang,[a]* Song Wang[a]* and Zhiyuan Tang

[a] College of Petroleum and Chemical Technology, Liaoning Petrochemical University, Fushun 113001, Liaoning, China

[b] Department of Applied Chemistry, School of Chemical Engineering and Technology, Tianjin University, Tianjin 300072, China

*Corresponding author:

Mrs. Lijuan Wang

E-mail address: lijuanw123@163.com

Tel.: +8624-56861711

Mr. Song Wang

E-mail address: wsong01@126.com

## Table of Contents

## I. Experimental

### Materials synthesis

$Li_2CO_3$, ZnO, $TiO_2$ and $(NH_4)_6Mo_7O_{24}\cdot 4H_2O$ were ball-milled at 400 rpm for 5 h in ethanol. The molar ratio of Li: Zn: Mo: Ti is 2.2: 1-x: x: 3 (x = 0, 0.05, 0.07, 0.09). The vessel of the ball-milling jar is 100 mL. The precursors were dried, ground and finally calcined for 4 h at 700 ℃ in air. The samples were marked as LZTO, LZM5TO, LZM7TO and LZM9TO, respectively. $Li_2ZnTi_{3-y}P_yO_8$ and $Li_2Zn_{1-x}Mo_xTi_{3-y}P_yO_8$ materials were prepared via the same processes. The molar ratio of Li: Zn: Ti: P is 2.2: 1: 3-y: y (y = 0.01, 0.03, 0.05) for $Li_2ZnTi_{3-y}P_yO_8$. The samples were marked as LZTP1O, LZTP3O and LZTP5O, respectively. The molar ratio of Li: Zn: Mo: Ti: P is 2.2: 0.93: 0.07: 2.97: 0.03 for $Li_2Zn_{1-x}Mo_xTi_{3-y}P_yO_8$. The sample was marked as LZM7TP3O.

### Physical and electrochemical measurements

Thermogravimetric (TG) analyses were conducted on a RD496 thermal analyzer at a heating rate of 10 °C $min^{-1}$ from room temperature to 800 °C in air. The phases were investigated via an X-ray diffraction technique conducted on a Bruker D8 Advance X-ray diffractometer with a Cu Kα radiation ($\lambda$ = 1.54 Å) in the 2$\theta$ ranges of 10-85 ° for $Li_2ZnTi_3O_8$ and 10-70 ° for $LiNi_{0.5}Mn_{1.5}O_4$ with the step of 0.02 °. The FullProf program is used for crystal structure refinements, employing the Rietveld method. The mass fractions of Mo and P in the final product of LZM7TP3O was calculated from elemental analysis by ICP (Inductive Coupled Plasma Emission Spectrometer, Agilent 725aes) measurement. The morphologies of the products were

observed by a SU8010 scanning electron microscope (SEM). The high-resolution transmission electron microscope (HR-TEM) (JEM-2100F) was used to observe the nanoscale microstructures. X-ray photoelectron spectroscopy (XPS) measurements (PHI 5600 CI, mono-chromatic Al-Ka radiation) were used to identify the surface species. The electronic conductivity of pristine and doped anodes was obtained from a powder resistivity tester (ST2722-SD).

The electrochemical measurements were performed in CR2025 coin-type cells. The working electrodes were composed of 85 wt.% active material, 10 wt.% conductive agent of acetylene black, and 5 wt.% binder of polyvinylidene difluoride (PVDF). The assembly of the cells was carried out in a glove box filled with high purity argon. For the half cells, $Li_2ZnTi_3O_8$ or $LiNi_{0.5}Mn_{1.5}O_4$ was used as the working electrode and the fresh lithium foil was used as the counter/reference electrode. The loading of the active materials is 2.8-3.0 mg $cm^{-2}$ for the half cells. For the full cells, $LiNi_{0.5}Mn_{1.5}O_4$ and $Li_2ZnTi_3O_8$ were used as the positive electrode and negative electrode, respectively. The specific capacities of the full cells are calculated based on the masses of the anode active materials. The electrolyte was 1.2 M $LiPF_6$ dissolved into a mixture of ethylene carbonate (EC) and ethyl methyl carbonate (EMC) with the volumetric ratio of 3:7. In this study, $LiNi_{0.5}Mn_{1.5}O_4$ was purchased from Shenzhen Biyuan Electronics Co., Ltd. Charge-discharge and cyclic voltammetry (CV) measurements were in the ranges of 0.02-3.0 V for $Li_2ZnTi_3O_8$/Li half cells, 3.5-4.95 V for $LiNi_{0.5}Mn_{1.5}O_4$/Li half cells, and 2-4.55 V for $LiNi_{0.5}Mn_{1.5}O_4/Li_2ZnTi_3O_8$ full cells. The scanning rates of CV measurements were 0.5, 0.1 and 0.1 mV $s^{-1}$ for

$Li_2ZnTi_3O_8$/Li half cells, $LiNi_{0.5}Mn_{1.5}O_4$/Li half cells, and $LiNi_{0.5}Mn_{1.5}O_4$/$Li_2ZnTi_3O_8$ full cells, respectively. Electrochemical impedance spectroscopies (EIS) were recorded with an *ac* voltage of 5 mV from 10 mHz to 100 kHz. The coin-type cells after cycling were transferred to a glove box and then dissembled. The electrodes were rinsed using dimethyl carbonate (DMC) to remove the electrolytes from the electrode surfaces. Then, electrodes were dried in the glove box antechamber to remove the residual DMC. The phases of the electrodes were investigated via an XRD technique.

**II. Supplementary Figs. 1-9 and Tables 1-5**

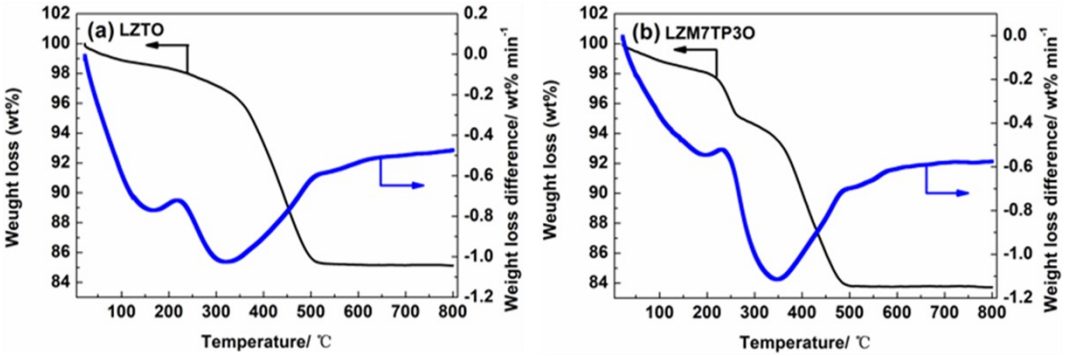


Fig. S1 TG-DTG curves of the precursors for (a) LZTO and (b) LZM7TP3O.

The thermogravimetric (TG) and differential thermogravimetric (DTG) curves of the precursors for LZTO and LZM7TP3O are shown in Fig. S1 at a heating rate of 10 °C $min^{-1}$ in air. The weight loss before 150 °C originates from the evaporation of absorbed water for the two precursors. The weight loss from 200 to 530 °C is related to the decomposition of $Li_2CO_3$ for the precursor of LZTO or $Li_2CO_3$, $(NH_4)_6Mo_7O_{24}{\cdot}4H_2O$ and $NH_4H_2PO_4$ for the precursor of LZM7TP3O. There is a platform on the TG curve above 530 °C, indicating the formation of LZTO or LZM7TP3O after this temperature. Based on the above analyses, we design an

optimal one-step sintering process at 700 °C for 4 h.

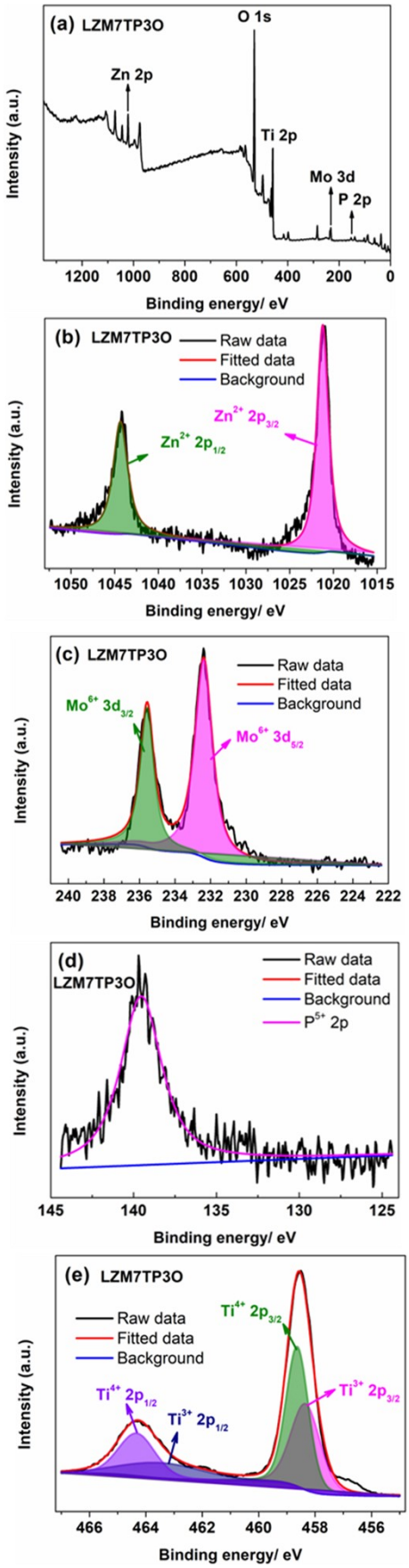

Fig. S2 (a) XPS spectrum of LZM7TP3O. High-resolution XPS spectra of LZM7TP3O for (b) Zn 2p, (c) Mo 3d, (d) P 2p and (e) Ti 2p.

The XPS spectrum of LZM7TP3O is shown in Fig. S2a. Mo and P elements exist in LZM7TP3O. Zn 2p spectrum consists of Zn $2p_{3/2}$ (1021.5 eV) and Zn $2p_{1/2}$ (1044.6 eV) (Fig. S2b). The major peaks at 253.6 and 232.4 eV (Fig. S2c) are attributed to $Mo^{6+}$ $3d_{5/2}$ and $Mo^{6+}$ $3d_{3/2}$, respectively [1, 2]. The peak located at 139.5 eV (Fig. S2d) is attributed to $P^{5+}$ 2p. The high-resolution XPS spectrum of Ti 2p displays two peaks located at 464.9 (Ti $2p_{1/2}$) and 458.7eV (Ti $2p_{3/2}$) (Fig. S2e), which are the binding energies of $Ti^{4+}$ in LZTO [3]. The peaks at 458.1 and 463.9 eV are assigned to $Ti^{3+}$ $2p_{3/2}$ and $Ti^{3+}$ $2p_{1/2}$ [4], respectively. That is to say, there are $Ti^{3+}$ ions on the surface of LZM7TP3O. Therefore, the extra charges of $Mo^{6+}$ and $P^{5+}$ should be compensated by the existence of $Ti^{3+}$, indicating that Mo and P elements have been doped into LZTO.

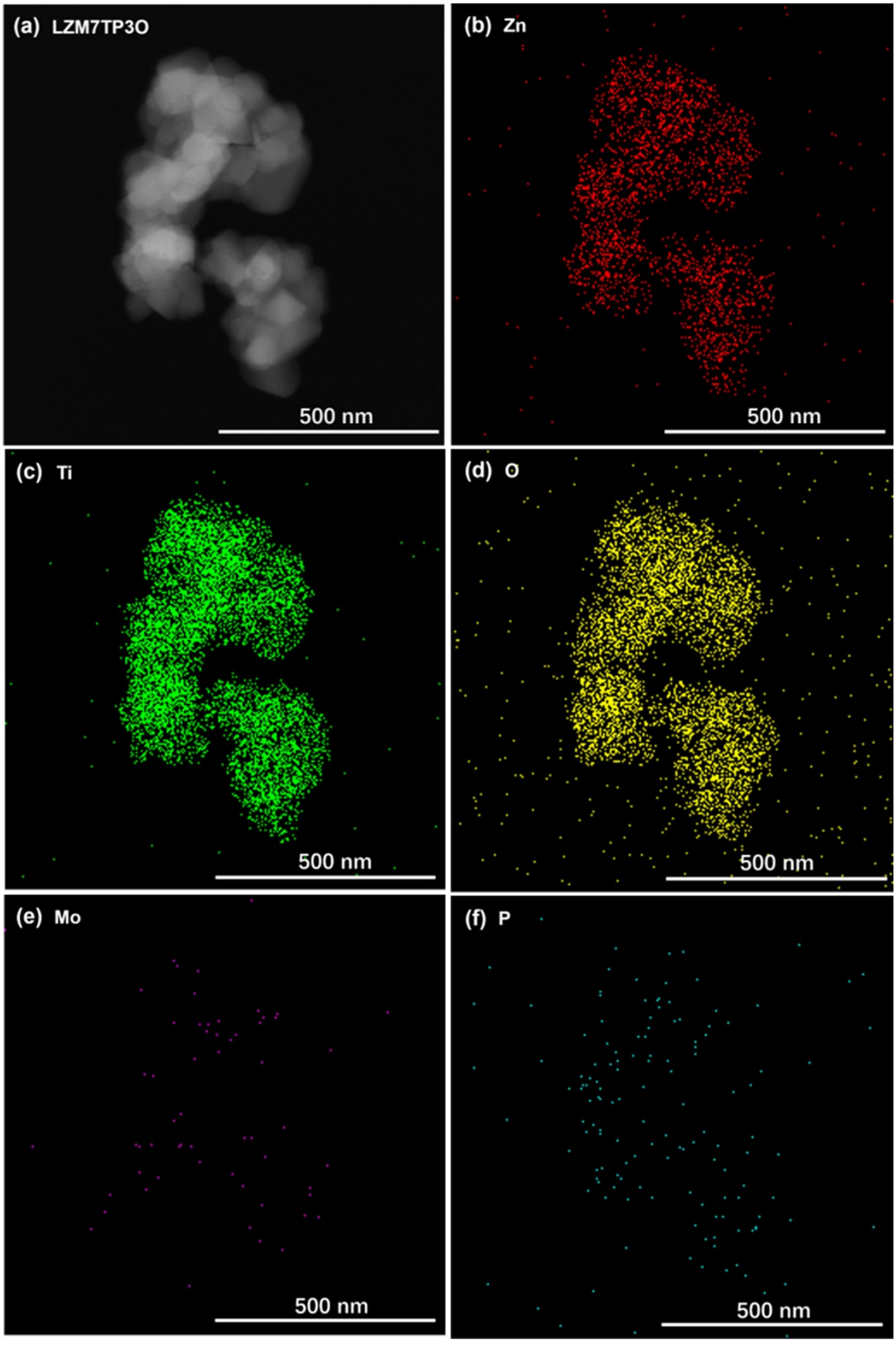


Fig. S3 (a) TEM image of LZM7TP3O. Elemental mappings of (b) Zn, (c) Ti, (d) O, (e) Mo and (f ) P in LZM7TP3O.

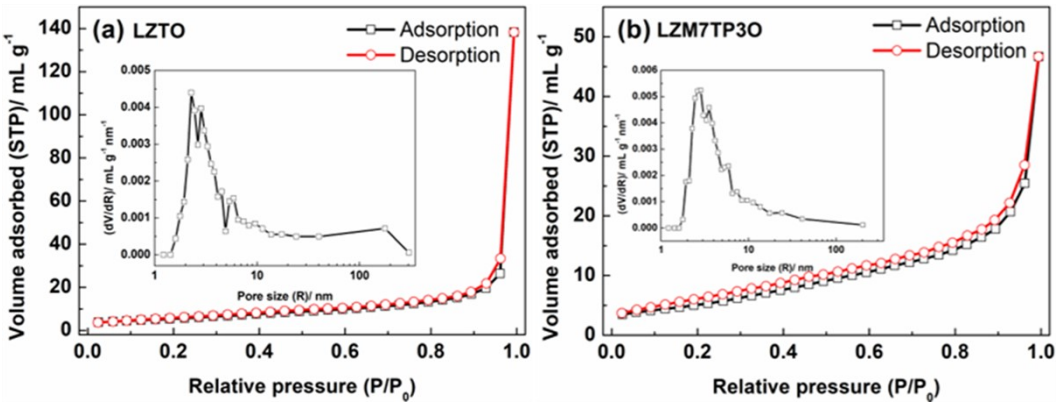


Fig. S4 $N_2$ adsorption-desorption isotherms of (a) LZTO and (b) LZM7TP3O (insets: pore size distributions).

Table S1 Specific surface areas and pore diameters of LZTO and LZM7TP3O.

| Samples | Specific surface areas ($m^2$ $g^{-1}$) | Pore diameters (nm) |
|---|---|---|
| LZTO | 21.4 | 2.28 |
| LZM7TP3O | 23.4 | 2.84 |

Table S2 Cyclic performance of LZTO corresponding to the 2nd cycle in recent publications.

| Materials | Current densities ($A\ g^{-1}$) | Cycle numbers | Capacity retention | References |
|---|---|---|---|---|
| $Li_2ZnTi_3O_8$@C | 0.229 | 100 | 99.2% | [5] |
| $Li_2ZnTi_3O_8$@C | 0.458 | 100 | 86.8% | [5] |
| C-LZTO | 0.458 | 200 | 91.3% | [6] |
| NC-LZTO | 0.458 | 200 | 99% | [6] |
| C-LZTO | 1.145 | 200 | 80.6% | [6] |
| NC-LZTO | 1.145 | 200 | 93.3% | [6] |
| LZTO-0 | 1 | 100 | 93.8% | [7] |
| LZTO-1 | 1 | 100 | 95.9% | [7] |
| LZTO-2 | 1 | 100 | 99.5% | [7] |
| LZTO-3 | 1 | 100 | 95.8% | [7] |
| LZTO-0 | 1 | 100 | 91.7% | [8] |
| LZTO-1 | 1 | 100 | 93.3% | [8] |
| LZTO-2 | 1 | 100 | 95.5% | [8] |
| LZTO-3 | 1 | 100 | 93.2% | [8] |
| $Li_2ZnTi_3O_8$ | 0.1 | 50 | 59.6% | [9] |
| $Li_2Zn_{0.5}Cu_{0.5}Ti_3O_8$ | 0.1 | 50 | 67.5% | [9] |
| LZTO | 1 | 500 | 64% | [10] |
| $Li_2Zn_{0.9}Cu_{0.1}Ti_3O_8$ | 0.1 | 80 | 93% | [11] |
| $Li_2Zn_{0.85}Cu_{0.15}Ti_3O_8$ | 0.1 | 80 | 98.5% | [11] |
| $Li_2ZnTi_3O_8$@$Li_2MoO_4$ | 1 | 500 | 86.3% | [12] |
| $Li_2ZnTi_3O_8$@$Li_2MoO_4$ | 0.5/2 | 500 | 75.7% | [12] |
| $Li_2ZnTi_3O_8$/$La_2O_3$ | 2 | 500 | 57.2% | [13] |
| $Li_2ZnTi_3O_8$ | 2 | 500 | 25% | [13] |
| $Li_2ZnTi_3O_8$/C@Cu | 1 | 600 | 67.6% | [14] |
| $Li_2ZnTi_3O_8$/C | 1 | 600 | 40.9% | [14] |
| $Li_2ZnTi_3O_8$/C@Cu | 2 | 500 | 56.5% | [14] |
| $Li_2ZnTi_3O_8$/C | 2 | 500 | 44.4% | [14] |
| $Li_2ZnTi_3O_8$ | 1 | 100 | 76.9% | [15] |
| $Li_2ZnTi_3O_8$ | 2 | 100 | 90.7% | [15] |
| $Li_2ZnTi_{2.9}Al_{0.1}O_8$ | 1 | 100 | 91.6% | [15] |
| $Li_2ZnTi_{2.9}Al_{0.1}O_8$ | 2 | 100 | 86.6% | [15] |
| $Li_2ZnTi_3O_8$/$LiCoO_2$ | 2 | 500 | 41.7% | [16] |
| $Li_2ZnTi_3O_8$ | 2 | 500 | 26.7% | [16] |
| $Li_2ZnTi_3O_8$ (COS) | 1 | 600 | 56.4% | [17] |
| $Li_2ZnTi_3O_8$ (PVDF) | 1 | 600 | 25% | [17] |
| $Li_2ZnTi_3O_8$ (COS) | 2 | 100 | 67.6% | [17] |
| $Li_2ZnTi_3O_8$ (PVDF) | 2 | 100 | 50.4% | [17] |
| $Li_2ZnTi_3O_8$ | 1 | 600 | 92.5% | [18] |
| $Li_2ZnTi_3O_8$ | 2 | 500 | 78.3% | [18] |
| LZTO | 1 | 100 | 91% | [19] |
| LZTO/C-1 | 1 | 100 | 92.4% | [19] |
| LZTO/C-2 | 1 | 100 | 94.8% | [19] |
| LZTO/C-3 | 1 | 100 | 79.8% | [19] |

Table S2 (Contd.)

| Materials | Current densities (A $g^{-1}$) | Cycle numbers | Capacity retention | References |
|---|---|---|---|---|
| Pristine Cu-LZTO | 1 | 200 | 86.9% | [20] |
| Bare Cu-LZTO | 1 | 200 | 87% | [20] |
| Cu-G-LZTO | 1 | 200 | 89.6% | [20] |
| Cu-G-Au-LZTO | 1 | 200 | 98.7% | [20] |
| Pristine Cu-LZTO | 2 | 200 | 75% | [20] |
| Bare Cu-LZTO | 2 | 200 | 85.1% | [20] |
| Cu-G-LZTO | 2 | 200 | 93.1% | [20] |
| Cu-G-Au-LZTO | 2 | 200 | 93.4% | [20] |
| LZTO-700-3 | 1 | 200 | 66.9% | [21] |
| LZTO@C-700-1 | 1 | 200 | 60.8% | [21] |
| LZTO@C-700-3 | 1 | 200 | 71.7% | [21] |
| LZTO@C-700-5 | 1 | 200 | 69.7% | [21] |
| LZTO-700-3 | 2 | 200 | 72.3% | [21] |
| LZTO@C-700-1 | 2 | 200 | 67.2% | [21] |
| LZTO@C-700-3 | 2 | 200 | 73.1% | [21] |
| LZTO@C-700-5 | 2 | 200 | 65.7% | [21] |
| LZTO@C-N-1 | 1 | 200 | 71.3% | [22] |
| LZTO@C-N-2 | 1 | 200 | 77.7% | [22] |
| LZTO@C-N-3 | 1 | 200 | 83.0% | [22] |
| LZTO@C-N-3 | 2 | 200 | 75.5% | [22] |
| LZTO | 1 | 200 | 68.5% | [23] |
| LZTO@C-N-1 | 1 | 200 | 61.8% | [23] |
| LZTO@C-N-2 | 1 | 200 | 68.1% | [23] |
| LZTO@C-N-3 | 1 | 200 | 63.8% | [23] |
| LZTO@C-N-2 | 2 | 200 | 73.7% | [23] |
| LZTO@C-N-2 | 3 | 200 | 75% | [23] |
| LZTO | 1 | 400 | 75.8% | [24] |
| LZTO/G | 1 | 400 | 76.4% | [24] |
| LZTO | 2 | 300 | 63.1% | [24] |
| LZTO/G | 2 | 300 | 72.3% | [24] |
| LZTO@GNS | 1 | 550 | 70.3% | [25] |
| LZTO@GNS-CNT | 1 | 550 | 81.3% | [25] |
| LZTO@GNS | 2 | 500 | 69% | [25] |
| LZTO@GNS-CNT | 2 | 500 | 91.8% | [25] |
| LZTO | 1 | 600 | 81.4% | [26] |
| LZTMO@G | 1 | 600 | 82.4% | [26] |
| LZTO | 2 | 300 | 57.2% | [26] |
| LZTMO@G | 2 | 300 | 89.7% | [26] |
| LZTO@C | 1 | 200 | 70.5% | [27] |
| LZTO@C | 2 | 200 | 65.7% | [27] |
| LZTO@C@$La_2O_3$ | 1 | 200 | 89.8% | [27] |
| LZTO@C@$La_2O_3$ | 2 | 200 | 77.2% | [27] |
| LZTO-0 | 1.5 | 500 | 89.3% | [3] |
| LZTO-1 | 1.5 | 500 | 90.5% | [3] |
| LZTO/NMO | 1 | 400 | 85.3% | [28] |
| $Li_2ZnAg_{0.15}Ti_{2.85}O_8$ | 1 | 100 | 91.4% | [29] |

Table S2 (Contd.)

| Materials | Current densities (A $g^{-1}$) | Cycle numbers | Capacity retention | References |
|---|---|---|---|---|
| $Li_2ZnAg_{0.15}Ti_{2.85}O_8$ | 2 | 100 | 82% | [29] |
| $Li_2ZnTi_3O_8$ | 1 | 100 | 83.1% | [29] |
| $Li_2ZnTi_3O_8$ | 2 | 100 | 99.2% | [29] |
| LZTO/C-3 | 1 | 500 | 94.4% | [30] |
| LZTO | 1 | 400 | 34.6% | [31] |
| LZTW3O | 1 | 400 | 93.1% | [31] |
| LM6ZTW3O | 1 | 400 | 94.7% | [31] |
| LZTN1O | 1 | 600 | 99.1% | [32] |
| LZM7TP3O | 1 | 600 | 109.5% | The work |
| LZM7TP3O | 1.5 | 500 | 101.1% | The work |
| LZM7TP3O | 2 | 500 | 98.2% | The work |

Table S3 Rate capability of LZTO in recent publications.

| Materials | Current densities (A $g^{-1}$) | Specific capacities (mAh $g^{-1}$) | Cycle numbers | References |
|---|---|---|---|---|
| $Li_2ZnTi_3O_8$@C | 2.29 | 190 | 35 | [5] |
| $Li_2ZnTi_3O_8$ | 2.29 | 189 | 35 | [5] |
| LZTO | 2.29 | 138.2 | 50 | [6] |
| C-LZTO | 2.29 | 180.9 | 50 | [6] |
| NC-LZTO | 2.29 | 190.6 | 50 | [6] |
| LZTO-0 | 2 | 75 | 50 | [7] |
| LZTO-1 | 2 | 140 | 50 | [7] |
| LZTO-2 | 2 | 170 | 50 | [7] |
| LZTO-3 | 2 | 168 | 50 | [7] |
| LZTO | 2 | 78 | 25 | [10] |
| $Li_2ZnTi_3O_8$@$Li_2MoO_4$ | 2 | 112 | 60 | [12] |
| $Li_2ZnTi_3O_8$ | 2 | 55 | 60 | [12] |
| $Li_2ZnTi_3O_8$/$La_2O_3$ | 3 | 149.3 | 40 | [13] |
| $Li_2ZnTi_3O_8$ | 3 | 116.9 | 40 | [13] |
| $Li_2ZnAg_{0.15}Ti_{2.85}O_8$ | 1.6 | 125 | 50 | [29] |
| $Li_2ZnTi_3O_8$ (COS) | 2 | 161 | 25 | [17] |
| $Li_2ZnTi_3O_8$ (PVDF) | 2 | 135.5 | 25 | [17] |
| $Li_2ZnTi_3O_8$ | 1.5 | 175 | 40 | [18] |
| $Li_2ZnTi_3O_8$ | 1.5 | 135 | 40 | [18] |
| $Li_2ZnTi_3O_8$ | 1.5 | 100 | 40 | [18] |
| LZTO-700-3 | 2.8 | 141.9 | 60 | [21] |
| LZTO@C-700-1 | 2.8 | 174.5 | 60 | [21] |
| LZTO@C-700-3 | 2.8 | 180.5 | 60 | [21] |
| LZTO@C-700-5 | 2.8 | 173.8 | 60 | [21] |
| $Li_2ZnTi_3O_8$ | 1.6 | 150 | 50 | [33] |
| $Li_2Mg_{0.5}Zn_{0.5}Ti_3O_8$ | 0.8 | 175 | 40 | [33] |
| $Li_2ZnTi_3O_8$/C | 2 | 145.6 | 50 | [34] |
| R-100-LZTO | 1.6 | 161.8 | 50 | [35] |
| R-10-LZTO | 1.6 | 147.1 | 50 | [35] |
| $Li_2ZnTi_3O_8$/$TiO_2$ | 2 | 173.4 | 50 | [36] |
| $Li_2ZnTi_3O_8$/$TiO_2$ | 3 | 161.6 | 60 | [36] |
| $Li_2ZnTi_{2.9}Al_{0.1}O_8$ | 1.6 | 131.8 | 50 | [15] |
| $Li_2ZnTi_3O_8$/C | 1.6 | 118 | 50 | [37] |
| $Li_2Zn_{0.6}Cu_{0.4}Ti_3O_8$ | 1 | 124.8 | 50 | [38] |
| $Li_2ZnTi_3O_8$ | 0.458 | 172.7 | 30 | [39] |
| $Li_2ZnTi_3O_8$/C-10 | 1.8 | 121.8 | 50 | [40] |
| LZTO | 1.145 | 47 | 106 | [41] |
| LZTO@RGO10 | 1.145 | 50 | 106 | [41] |
| LZTO@RGO25 | 1.145 | 154 | 106 | [41] |
| LZTO@RGO50 | 1.145 | 113 | 106 | [41] |
| C&N coated $Li_2ZnTi_3O_8$ | 2.5 | 190.6 | 40 | [42] |
| $Li_{1.95}Na_{0.05}ZnTi_3O_8$ | 0.458 | 162.3 | 80 | [43] |
| LTO-MB-05 | 2.29 | 100 | 20 | [44] |
| LZTO-2 | 2.29 | 135 | 20 | [45] |
| LZTNO | 1.145 | 80 | 15 | [46] |
| $Li_2ZnTi_3O_8$/C | 2 | 178 | 60 | [47] |

Table S3 (Contd.)

| Materials | Current densities (A $g^{-1}$) | Specific capacities (mAh $g^{-1}$) | Cycle numbers | References |
|---|---|---|---|---|
| $Li_2Zn_{0.9}Cu_{0.1}Ti_3O_8$ | 1 | 165.4 | 50 | [11] |
| LZTO/KCl | 1.6 | 135.6 | 50 | [48] |
| P-LZTO | 1.6 | 53.3 | 40 | [28] |
| LZTO/NMO | 1.6 | 161.3 | 40 | [28] |
| LZTO/NMO-1 | 1.6 | 101.8 | 40 | [28] |
| P-LZTO | 1.6 | 44 | 50 | [49] |
| LZTO/LMS-1 | 1.6 | 107.1 | 50 | [49] |
| LZTO/LMS-2 | 1.6 | 140.4 | 50 | [49] |
| LZTO/LMS-3 | 1.6 | 144.9 | 50 | [49] |
| PZ | 1.6 | 69.3 | 50 | [50] |
| FA1 | 1.6 | 124.5 | 50 | [50] |
| FA2 | 1.6 | 144.3 | 50 | [50] |
| FA3 | 1.6 | 96.1 | 50 | [50] |
| FA2-800 | 1.6 | 143.5 | 50 | [50] |
| FA2-850 | 1.6 | 127.6 | 50 | [50] |
| P-LZTO | 1.6 | 32.4 | 50 | [51] |
| LZTO/LZO | 1.6 | 109.8 | 50 | [51] |
| LZTO/LZO-1 | 1.6 | 85.3 | 50 | [51] |
| P-LZTO | 1.6 | 65.8 | 50 | [52] |
| LZTO/C-1 | 1.6 | 55.6 | 50 | [52] |
| LZTO/C-2 | 1.6 | 106.7 | 50 | [52] |
| LZTO/C-3 | 1.6 | 102.5 | 50 | [52] |
| $Li_2ZnTi_{2.9}Cr_{0.1}O_8$ | 2 | 156.7 | 50 | [53] |
| LM6ZTW3O | 2 | 199 | 80 | [31] |
| LM6ZTW3O | 2.5 | 191.7 | 100 | [31] |
| LM6ZTW3O | 3 | 177.9 | 120 | [31] |
| LZTO/C-3 | 2 | 169.8 | 40 | [30] |
| LZTO/C-3 | 3 | 150.9 | 50 | [30] |
| LZTO-E | 2 | 138 | 40 | [54] |
| LZTO-E | 3 | 125 | 50 | [54] |
| $Li_2ZnAg_{0.15}Ti_{2.85}O_8$ | 1.6 | 125 | 50 | [29] |
| $Li_2Zn_{0.9}Nb_{0.1}Ti_3O_8$ | 2 | 160 | 40 | [55] |
| $Li_2Zn_{0.9}Nb_{0.1}Ti_3O_8$ | 3 | 147 | 50 | [55] |
| FLZTO-2 | 1 | 179.4 | 60 | [56] |
| NWLZTO-2 | 1 | 132.8 | 60 | [57] |
| $Li_{1.95}V_{0.05}ZnTi_3O_8$ | 1.145 | 84.7 | 100 | [58] |
| LZM7TP3O | 1.5 | 210.3 | 60 | The work |
| LZM7TP3O | 2 | 201.8 | 80 | The work |
| LZM7TP3O | 2.5 | 191.9 | 100 | The work |
| LZM7TP3O | 3 | 180.5 | 120 | The work |

Table S4 Rate capability of some other anodes with comparable theoretical specific capacity with LZTO in recent publications.

| Materials | Current densities (A $g^{-1}$/C) | Specific capacities (mAh $g^{-1}$) | Cycle numbers | References |
|---|---|---|---|---|
| $TiO_2$@HCNs | 10 C | 186 | 50 | [59] |
| $TiO_2$@C | 5 C | 90 | 30 | [60] |
| $TiO_2$-carbonized PAN | 1 | 74.7 | 40 | [61] |
| $TiO_2$@rGO | 10 C | 85.6 | 40 | [62] |
| $TiO_2$ | 0.185 | 152 | 100 | [63] |
| 7% Co-doped $TiO_2$ | 5 C | 70 | 30 | [64] |
| $TiO_2$ (300) | 1 | 167 | 12 | [65] |
| $TiO_2$-B | 10 C | 181.3 | 50 | [66] |
| $TiO_2$-B-graphene | 5 C | 185 | 30 | [67] |
| $TiO_2$-B/$MoS_2$ | 10 C | 158 | 60 | [68] |
| $TiO_2$-B@$VS_2$ | 10 C | 171.2 | 50 | [69] |
| $TiNb_6O_{17}$ | 5 C | 127.3 | 80 | [70] |
| $Ti_2Nb_{10}O_{29}$ | 10 C | 176 | 1 | [71] |
| $Ti_2Nb_{10}O_{29}$/Ag | 10 C | 172 | 30 | [72] |
| $TiNb_2O_7$ | 1.6 | 145.7 | 50 | [73] |
| $TiNb_2O_7$ | 6 C | 183 | 35 | [74] |
| $Nb_2O_5$/$TiNb_2O_7$ | 10 C | 168 | 60 | [75] |
| $Ti_2Nb_{10}O_{29}$ | 10 C | 179.1 | 40 | [76] |
| $Ti_{0.98}Nb_{2.02}O_7$ | 5 C | 153 | 60 | [77] |
| $Li_3VO_4$ | 2 | 110 | 25 | [78] |
| $Li_3VO_4$ | 3 | 69 | 30 | [78] |
| $Li_3VO_4$ | 0.2 C | 168 | 10 | [79] |
| Li3VO4@C | 2 | 141 | 1 | [80] |
| LZM7TP3O | 2 (8.7 C) | 201.8 | 80 | The work |
| LZM7TP3O | 2.5 (10.9 C) | 191.9 | 100 | The work |
| LZM7TP3O | 3 (13.1 C) | 180.5 | 120 | The work |

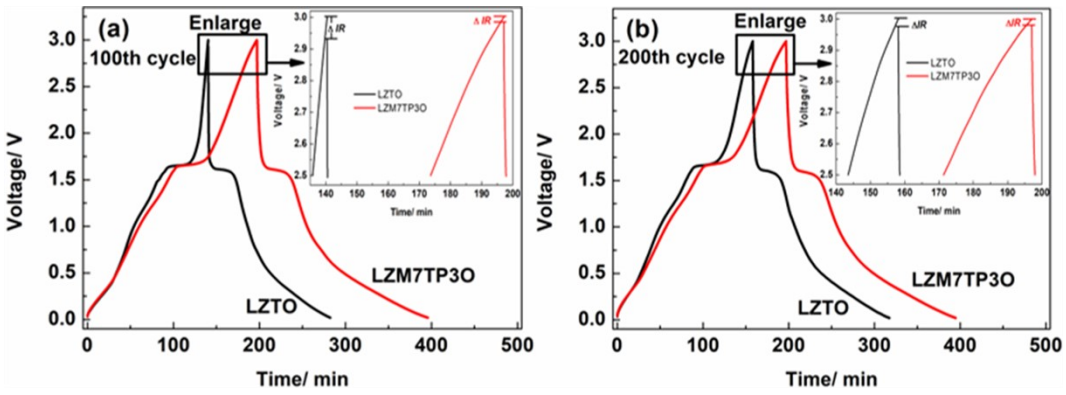


Fig. S5 IR-drop data of LZTO and LZM7TP3O electrodes at 0.1 A $g^{-1}$ when charging

is switched to discharging for the (a) 100th cycle and (b) 200th cycle.

The magnitude of internal resistance can be characterized by the voltage drop, or IR drop, when charging/discharging is switched to discharging/charging (Fig. S5). Compared with LZTO, LZM7TP3O has smaller IR drop during the cycling process.

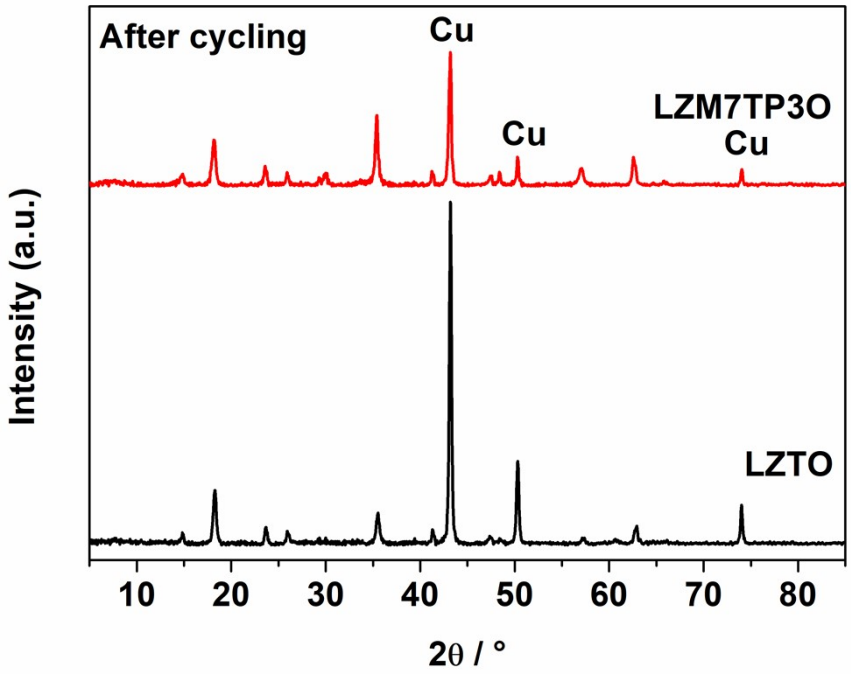


Fig. S6 Ex-situ XRD patterns of the LZTO and LZM7TP3O electrodes after cycling for 200 cycles at 1 A $g^{-1}$.

Fig. S6 presents the XRD patterns of the LZTO and LZM7TP3O electrodes after cycling for 200 cycles at 1 A $g^{-1}$. The diffraction peaks of the LZM7TP3O electrode are still sharp after cycling, indicating that the structure of the LZM7TP3O retains significantly stability during insertion and de-insertion of $Li^+$ ions. However, some of the diffraction peaks for the LZTO electrode are blurry, indicating that the structure of the LZTO is partly destroyed during cycling process.

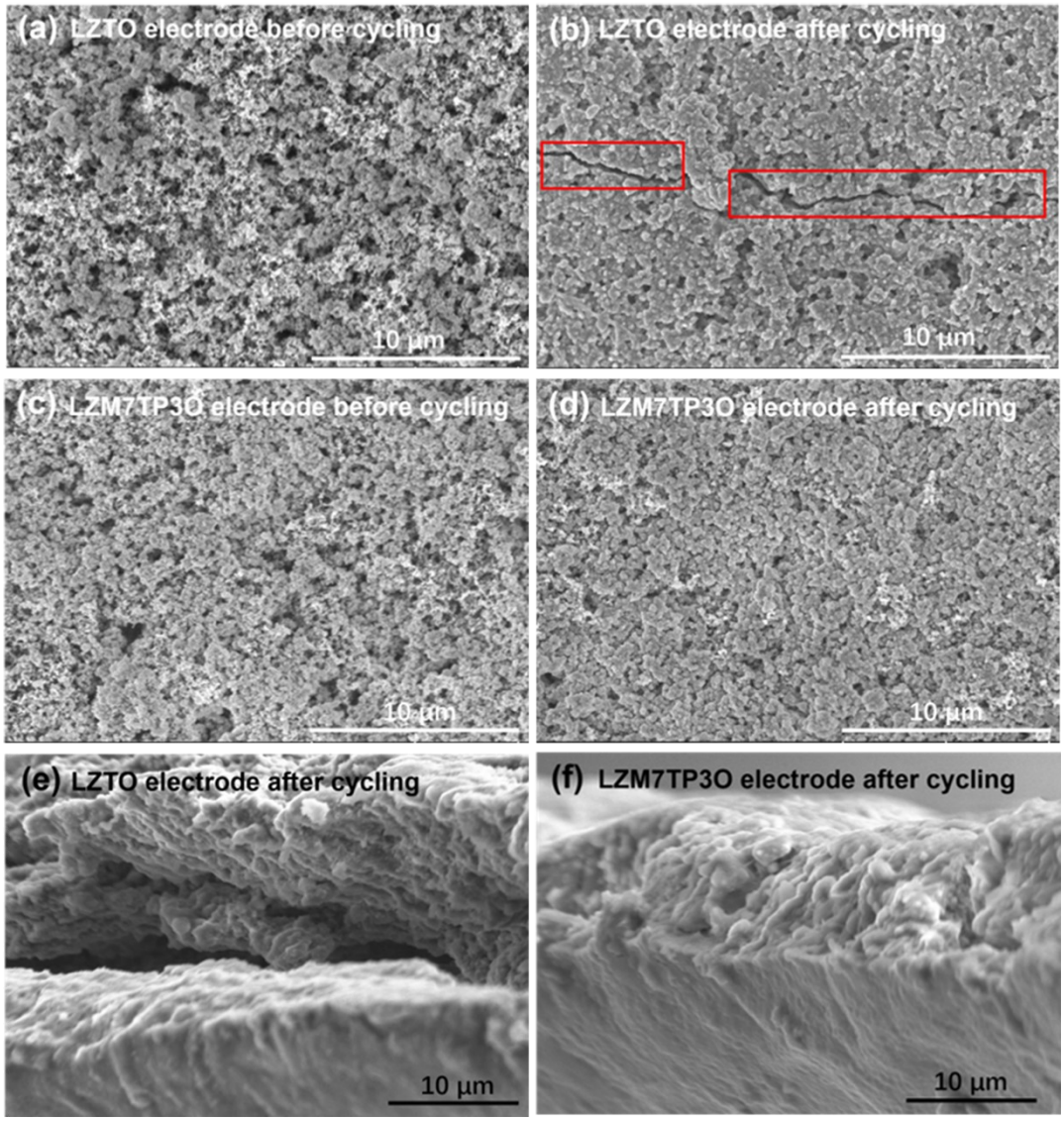


Fig. S7 Surface SEM images of (a-b) LZTO, and (c-d) LZM7TP3O before and after cycling for 200 cycles at 1 A $g^{-1}$. Cross-sectional SEM images of (e) LZTO, and (f) LZM7TP3O after cycling for 200 cycles at 1 A $g^{-1}$.

The SEM images of the LZTO and LZM7TP3O electrodes before and after cycling for 200 cycles at 1 A $g^{-1}$, are shown in Fig. S7. The surface of the LZTO electrode is severely damaged after repeated $Li^+$ insertion/de-insertion, and some cracks appear (Fig. S7b). The cracks will prevent the transportation of electrons and the diffusion of $Li^+$ ions, and then lead to the capacity fading. However, there is no

obvious crack on the surface of LZM7TP3O (Fig. S7d). The integrated surface can keep good electrical contact between active particles. From the cross-sectional SEM images as shown in Figs. S7e-f, compared with the LZM7TP3O electrode, the detachment of the active material layer from the Cu substrate is more pronounced for the LZTO electrode, indicating the better adhesion between LZM7TP3O and the current collector. This strong adhesion helps to maintain a good electrical contact between the current collector and LZM7TP3O.

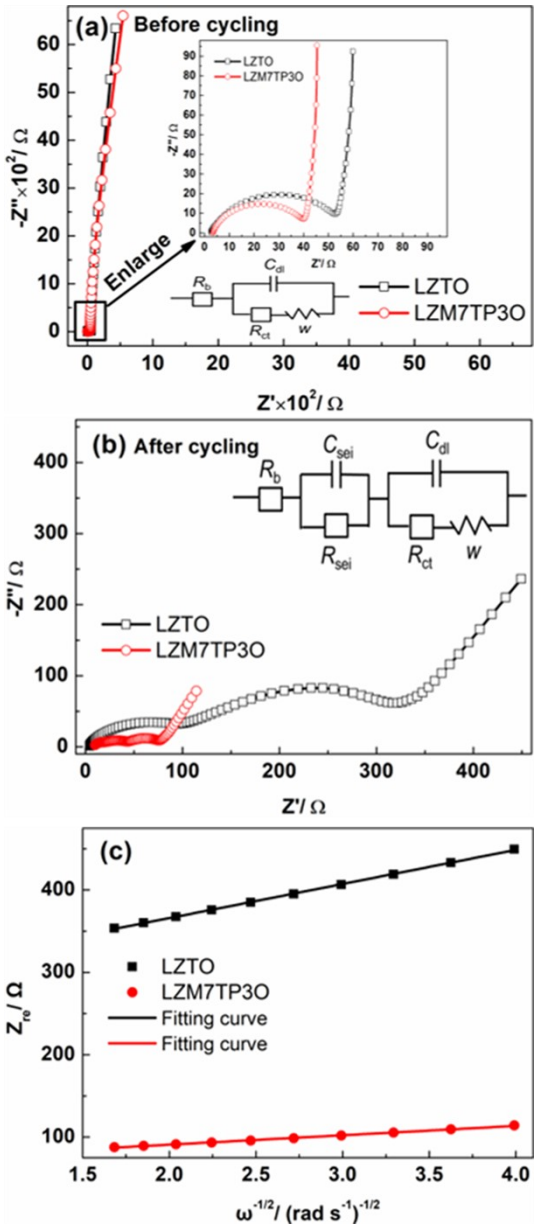


Fig. S8 Impedance spectra of the LZTO and LZM7TP3O electrodes (a) before cycling and (b) after cycling at different current densities in Fig. 5d and corresponding equivalent circuits (inset). (c) Relationship between $Z_{re}$ and $\omega^{-1/2}$.

The electrochemical impedance data were collected on as assembled cells before and after cycling at different current densities in Fig. 5d and are presented in Figs. S8a-b. The potentials are *ca*. 2 V. The curves are similar for the two electrodes, composed of a small intercept, one semicircle and a straight line for each electrode

before cycling. The equivalent circuit model is shown in Fig. S8a (inset). $R_b$ is the combined impedance of the electrolyte and cell components; $C_{dl}$ and $R_{ct}$, are the double layer capacitance and charge transfer resistance; $W$ represents Warburg impedance. The charge transfer resistance is 29.95 and 21.99 Ω for LZTO and LZM7TP3O (Table S5), respectively. When the two electrodes were cycled at different current densities, there are two semicircles on the impedance spectra. The equivalent circuit model is shown in Fig. S8b (inset). $C_{sei}$ and $R_{sei}$ represent the capacitance and the resistance of the SEI (solid electrolyte interface) layer for the first semicircle; $C_{dl}$ and $R_{ct}$ correspond to the second semicircle. The charge transfer resistance is 155 and 28.73 Ω for LZTO and LZM7TP3O (Table S5), respectively. The charge transfer resistance decreases after doping. Small charge transfer resistance is advantageous to the electrochemical performance.

To further investigate the electrode kinetics, the diffusion coefficients of $Li^+$ ions in the two samples are estimated based on the Warburg diffusion in low frequency (Fig. S8b) using the following equation [38]

$$D_{Li^+} = R^2T^2 / (2A^2n^4F^4C^2\sigma^2) \quad \text{(S1)}$$

where $R$ is the gas constant (8.314 J $mol^{-1}$ $K^{-1}$); $T$ is the room absolute temperature (298.5 K); $A$ is the surface area of the electrode (1.13 $cm^2$ in this work); $n$ is the number of electrons transferred in the half reaction for the redox couple; $F$ is Faraday constant (96,485 C $mol^{-1}$); $C$ is the concentration of $Li^+$ ion in the compound, and can be calculated based on the following equation

$$C = \frac{3 \times 4}{6.022 \times 10^{23} \times V} \quad \text{(S2)}$$

$\sigma$ is the Warburg factor which obeys the following relationship:

$$Z_{re} = R_e + R_{ct} + \sigma\omega^{-1/2} \quad \text{(S3)}$$

Fig. S8c shows the relationship between $Z_{re}$ and $\omega^{-1/2}$. Based on the Equations S1 and S3, the lithium diffusion coefficients ($D_{Li}^{+}$) of LZTO and LZM7TP3O can be calculated and the specific values are $1.12\times10^{-10}$ and $1.47\times10^{-9}$ $cm^2$ $s^{-1}$, respectively. Compared with LZTO electrode, Mo-P co-doped LZTO material has high $D_{Li}^{+}$, which indicates the fast diffusion of $Li^+$ ions and thus guarantees good rate capability.

Table S5 Impedance parameters calculated from equivalent circuit model, lithium diffusion coefficients ($D_{Li}^{+}$) and electronic conductivity of LZTO and LZM7TP3O.

| Samples | Before cycling | | After cycling | | | $D_{Li+}$ ($cm^2$ $s^{-1}$) | $\sigma$ (S $cm^{-1}$) |
|---|---|---|---|---|---|---|---|
| | $R_b$ (Ω) | $R_{ct}$ (Ω) | $R_b$ (Ω) | $R_{sei}$ (Ω) | $R_{ct}$ (Ω) | | |
| LZTO | 3.411 | 29.95 | 6.079 | 78.64 | 155 | $1.12\times10^{-10}$ | $3.89\times10^{-5}$ |
| LZM7TP3O | 3.838 | 21.99 | 11.421 | 17.74 | 28.73 | $1.47\times10^{-9}$ | $6.91\times10^{-5}$ |

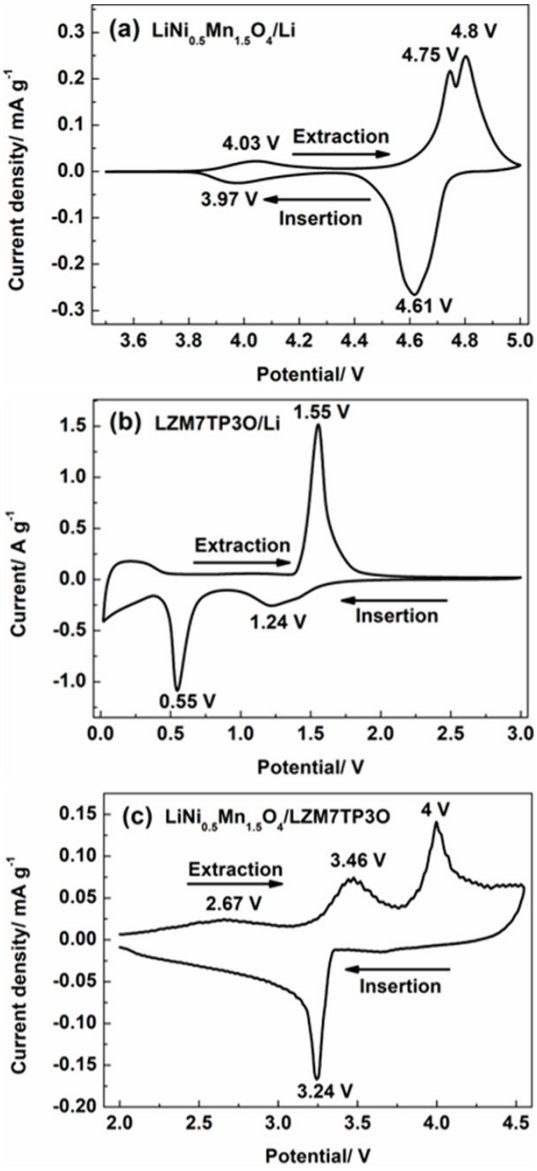


Fig. S9 Cyclic voltammograms of (a) $LiNi_{0.5}Mn_{1.5}O_4$/Li, (b) LZM7TP3O/Li and (c) $LiNi_{0.5}Mn_{1.5}O_4$/LZM7TP3O.

Fig. S9 shows the cyclic voltammograms of $LiNi_{0.5}Mn_{1.5}O_4$/Li, LZM7TP3O /Li and $LiNi_{0.5}Mn_{1.5}O_4$/LZM7TP3O in 3.5-5.0 V, 0.02-3 V and 2-4.55 V, respectively. For $LiNi_{0.5}Mn_{1.5}O_4$/Li (Fig. S9a), the peaks at 4.03/3.97 V are due to $Mn^{4+}/Mn^{3+}$ redox couple, and the peaks at 4.75 (4.80)/4.61 V are due to $Ni^{3+}/Ni^{2+}$ and $Ni^{4+}/Ni^{3+}$, respectively. For LZM7TP3O/Li (Fig. S9b), a pair of redox peaks appears at 1.24/1.55 V, which can be attributed to the redox of $Ti^{4+}/Ti^{3+}$ couple. Moreover, a

reduction peak *ca*. 0.5 V is observed. There are three oxidation peaks at 2.67, 3.46 and 4 V, and one sharp reduction peak at 3.24 V for the $LiNi_{0.5}Mn_{1.5}O_4$/LZM7TP3O full cell (Fig. S9c). $Li^+$ ions can be inserted/de-inserted to the maximum extent in the range of 2.0-4.55 V for the $LiNi_{0.5}Mn_{1.5}O_4$/LZM7TP3O full cell. In addition, the potential window will not cause a lot of side reactions between active materials and electrolytes.

## Ⅲ. References


[1] T. Sattar, S.-H. Lee, B.-S. Jin, H.-S. Kim, Infuence of Mo addition on the structural and electrochemical performance of Ni-rich cathode material for lithium-ion batteries, Scientific Reports, 10 (2020) 8562-8571.

[2] H. Zhu, H. Yu, H. Jiang, Y. Hu, H. Jiang, C. Li, High-efficiency Mo doping stabilized $LiNi_{0.9}Co_{0.1}O_2$ cathode materials for rapid charging and long-life Li-ion batteries, Chemical Engineering Science, 217 (2020) 115518-115525.

[3] C. Chen, C. Ai, X. Liu, Ti(III) self-doped $Li_2ZnTi_3O_8$ as a superior anode material for Li-ion batteries, Electrochimica Acta, 265 (2018) 448-454.

[4] K. Liang, X. Huang, X. Hong, Y. Liao, Y. Ren, H. Wang, Sulfur and nitrogen-doped $Li_4Ti_5O_{12}$/rGO as an anode material for advanced sodium-ion batteries, Journal of Alloys and Compounds, 857 (2021) 158190-158198.

[5] C. Chen, C. Ai, X. Liu, Y. He, S. Yang, Y. Wu, High performance $Li_2ZnTi_3O_8$@C anode material fabricated by a facile method without an additional carbon source, Journal of Alloys and Compounds, 698 (2017) 692-698.

[6] X. Liu, C. Chen, Y. Wu, Investigation of N-doped carbon-coated lithium zinc

titanate using chitin as a carbon source for lithium-ion batteries, Ionics, 23 (2016) 889-896.

[7] Y. Ren, P. Lu, X. Huang, J. Ding, H. Wang, Synthesis and high cycle performance of $Li_2ZnTi_3O_8$/C anode material promoted by asphalt as a carbon precursor, RSC Advances, 6 (2016) 49298-49306.

[8] Y. Ren, P. Lu, X. Huang, J. Ding, H. Wang, Enhanced electrochemical properties of $Li_2ZnTi_3O_8$/C nanocomposite synthesized with phenolic resin as carbon source, Journal of Solid State Electrochemistry, 21 (2017) 125-131.

[9] W. Chen, H. Liang, W. Ren, L. Shao, J. Shu, Z. Wang, Complex spinel titanate as an advanced anode material for rechargeable lithium-ion batteries, Journal of Alloys and Compounds, 611 (2014) 65-73.

[10] A. I. Inamdar, A. T. A. Ahmed, H. S. Chavan, Y. Jo, S. Cho, J. Kim, S. M. Pawar, B. Hou, S. N. Cha, H. Kim, H. Im, Inflfluence of operating temperature on $Li_2ZnTi_3O_8$ anode performance and high-rate charging activity of Li-ion battery, Ceramics International, 44 (2018) 18625-18632.

[11] F. Qie, Z. Tang, Cu-doped $Li_2ZnTi_3O_8$ anode material with improved electrochemical performance for lithium-ion batteries, Materials Express, 4 (2014) 221-227.

[12] Z. Li, H. Li, Y. Cui, Z. Du, Y. Ma, C. Ma, Z. Tang, $Li_2MoO_4$ modified $Li_2ZnTi_3O_8$ as a high property anode material for lithium ion battery, Journal of Alloys and Compounds, 692 (2017) 131-139.

[13] H. Tang, L. Zan, J. Zhu, Y. Ma, N. Zhao, Z. Tang, High rate capacity nanocomposite lanthanum oxide coated lithium zinc titanate anode for rechargeable lithium-ion battery, Journal of Alloys and Compounds, 667 (2016) 82-90.

[14] H. Tang, Y. Zhou, L. Zan, N. Zhao, Z. Tang, Long cycle life of carbon coated lithium zinc titanate using copper as conductive additive for lithium ion batteries, Electrochimica Acta, 191 (2016) 887-894.

[15] H. Tang, J. Zhu, Z. Tang, C. Ma, Al-doped $Li_2ZnTi_3O_8$ as an effective anode material for lithium-ion batteries with good rate capabilities, Journal of Electroanalytical Chemistry, 731 (2014) 60-66.

[16] H. Tang, J. Zhu, C. Ma, Z. Tang, Lithium cobalt oxide coated lithium zinc titanate anode material with an enhanced high rate capability and long lifespan for lithium-ion batteries, Electrochimica Acta, 144 (2014) 76-84.

[17] H. Tang, Q. Weng, Z. Tang, Chitosan oligosaccharides: A novel and efficient water soluble binder for lithium zinc titanate anode in lithium-ion batteries, Electrochimica Acta, 151 (2015) 27-34.

[18] T. Liu, H. Tang, L. Zan, Z. Tang, Comparative study of $Li_2ZnTi_3O_8$ anode material with good high rate capacities prepared by solid state, molten salt and sol–gel methods, Journal of Electroanalytical Chemistry, 771 (2016) 10-16.

[19] L. Wang, B. Chen, Z. Meng, B. Luo, X. Wang, Y. Zhao, High performance carbon-coated lithium zinc titanate as an anode material for lithium-ion batteries, Electrochimica Acta, 188 (2016) 135-144.

[20] X. Li, L. Wang, C. Li, B. Chen, Q. Zhao, G. Zhang, Rational design of high-rate

lithium zinc titanate anode electrode by modifying Cu current collector with graphene and Au nanoparticles, Journal of Power Sources, 308 (2016), 65-74.

[21] Z. Meng, L. Wang, X. Li, G. Zhang, H. Li, Synthesis of high performance carbon-coated lithium zinc titanate via an EDTA-assisted route, International Journal of Hydrogen Energy, 42 (2017) 2177-2186.

[22] Z. Meng, S. Wang, X. Chen, L. Wang, F. Wang, Synthesis high rate capability N-doped carbon coated on lithium zinc titanate via a surfacant-assisted solid-state, RSC Advances, 7 (2017) 54258-54265.

[23] Z. Meng, S. Wang, L. Wang, H. Hou, Synthesis of high performance N-doped carbon coated $Li_2ZnTi_3O_8$ via a NTA-assisted solid-state route, Dalton Transactions, 47 (2018) 2711-2718.

[24] S. Wang, L. Wang, Z. Meng, B. Luo, $Li_2ZnTi_3O_8$/graphene nanocomposite as a high-performance anode material for lithium-ion batteries, RSC Advances, 8 (2018) 31628-31632.

[25] S. Wang, L. Wang, Z. Meng, R. Xun, Design of a three-dimensional-network $Li_2ZnTi_3O_8$ co-modified with graphene nanosheets and carbon nanotubes as a high performance anode material for lithium-ion batteries, Journal of Alloys and Compounds, 774 (2019) 581-585.

[26] S. Wang, Y. Bi, L. Wang, Z. Meng, B. Luo, Mo-doped $Li_2ZnTi_3O_8$@graphene as a high performance anode material for lithium-ion batteries, Electrochimica Acta, 301 (2019) 319-324.

[27] Z. Meng, S. Wang, H. Wang, L. Wang, S. Wang, $La_2O_3$-coated $Li_2ZnTi_3O_8$@C

as a high performance anode for lithium-ion batteries, RSC Advances, 9 (2019) 20618-20623.

[28] H. Yang, J. Park, C.S. Kim, Y.H. Xu, H.L. Zhu, Y.X. Qi, L. Yin, H. Li, N. Lun, Y.J. Bai, Uniform surface modification of $Li_2ZnTi_3O_8$ by liquated $Na_2MoO_4$ to boost electrochemical performance, ACS Appllied Materials & Interfaces, 9 (2017) 43603-43613.

[29] H. Tang, Z. Tang, C. Du, F. Qie, J. Zhu, Ag-doped $Li_2ZnTi_3O_8$ as a high rate anode material for rechargeable lithium-ion batteries, Electrochimica Acta, 120 (2014) 187-192.

[30] H. Tang, C. Chen, T. Liu, Z. Tang, Chitosan and chitosan oligosaccharide: Advanced carbon sources are used for preparation of N-doped carbon-coated $Li_2ZnTi_3O_8$ anode material, Journal of Electroanalytical Chemistry, 858 (2020) 113789-113797.

[31] Z. Shen, Z. Zhang, S. Wang, Z. Liu, L. Wang, Y. Bi, Z. Meng, $Mg^{2+}$–$W^{6+}$ co-doped $Li_2ZnTi_3O_8$ anode with outstanding room, high and low temperature electrochemical performance for lithium-ion batteries, Inorganic Chemistry Frontiers, 6 (2019) 3288-3294.

[32] Z. Zhang, R. Xun, Z. Shen, L. Wang, S. Wang, Z. Meng, Synthesis of Nb-doped $Li_2ZnTi_3O_8$ anode with long cycle life and applications in the $LiMn_2O_4$/$Li_2ZnTi_3O_8$ full cell, ACS Sustainable Chemistry & Engineering, 8 (2020) 2763-2771.

[33] Z. Hong, T. Lan, Y. Zheng, L. Jiang, M. Wei, Spinel $Li_2MTi_3O_8$ (M = Mg, $Mg_{0.5}Zn_{0.5}$) nanowires with enhanced electrochemical lithium storage, Functional

Materials Letters, 04 (2011) 65-69.

[34] Y. Xu, Z. Hong, L. Xia, J. Yang, M. Wei, One step sol–gel synthesis of $Li_2ZnTi_3O_8$/C nanocomposite with enhanced lithium-ion storage properties, Electrochimica Acta, 88 (2013) 74-78.

[35] L. Wang, Z. Meng, H. Wang, X. Li, G. Zhang, Effects of $TiO_2$ starting materials on the synthesis of $Li_2ZnTi_3O_8$ for lithium ion battery anode, Ceramics International, 42 (2016) 16872-16881.

[36] H. Li, Z. Li, Y. Cui, C. Ma, Z. Tang, Long-cycled $Li_2ZnTi_3O_8$/$TiO_2$ composite anode material synthesized via a one-pot co-precipitation method for lithium ion batteries, New Journal of Chemistry, 41 (2017) 975-981.

[37] H. Tang, Z. Tang, Effect of different carbon sources on electrochemical properties of $Li_2ZnTi_3O_8$/C anode material in lithium-ion batteries, Journal of Alloys and Compounds, 613 (2014) 267-274.

[38] Y. Li, C. Du, J. Liu, F. Zhang, Q. Xu, D. Qu, X. Zhang, Z. Tang, Synthesis and characterization of $Li_2Zn_{0.6}Cu_{0.4}Ti_3O_8$ anode material via a sol-gel method, Electrochimica Acta, 167 (2015) 201-206.

[39] L. Wang, L. Wu, Z. Li, G. Lei, Q. xiao, P. Zhang, Synthesis and electrochemical properties of $Li_2ZnTi_3O_8$ fibers as an anode material for lithium-ion batteries, Electrochimica Acta, 56 (2011) 5343-5346.

[40] H. Tang, L. Zan, W. Mao, Z. Tang, Improved rate performance of amorphous carbon coated lithium zinc titanate anode material with alginic acid as carbon precursor and particle size controller, Journal of Electroanalytical Chemistry, 751

(2015) 57-64.

[41] S. Yıldız, H. Şahan, In situ synthesis of reduced graphite oxide-$Li_2ZnTi_3O_8$ composite as a high rate anode material for lithium-ion batteries, Journal of The Electrochemical Society, 166 (2019) A2002-A2012.

[42] C. Chen, Z. Li, B. Xu, Surface modification of $Li_2ZnTi_3O_8$ with the C&N layer for lithium-ion batteries, Materials Chemistry and Physics, 245 (2020) 122718-122725.

[43] W. Chen, Z. Zhou, R. Wang, Z. Wu, H. Liang, L. Shao, J. Shu, Z. Wang, High performance Na-doped lithium zinc titanate as anode material for Li-ion batteries, RSC Advances, 5 (2015) 49890-49898.

[44] N. Firdous, N. Arshad, N. Muzaffar, P. Norby, Effect of $Mg^{+2}$ and $B^{i+3}$ co-doping on structural and electrochemical properties of lithium titanium oxide for use as anode material in lithium-ion battery, Journal of Electroanalytical Chemistry, 876 (2020) 114515-114522.

[45] N. Firdous, N. Arshad, P. Norby, Synergic effect of niobium doping and carbon coating on the performance of a $Li_2ZnTi_3O_8$ anode candidate for lithium ion batteries, Energy & Fuels, 34 (2020) 14968-14974.

[46] N. Firdous, N. Arshad, S.B. Simonsen, P. Kadirvelayutham, P. Norby, Advanced electrochemical investigations of niobium modified $Li_2ZnTi_3O_8$ lithium ion battery anode materials, Journal of Power Sources, 462 (2020) 228186-228195.

[47] T. Lan, L. Chen, Y. Liu, W. Zhang, M. Wei, Nanocomposite $Li_2ZnTi_3O_8$/C with enhanced electrochemical performances for lithium-ion batteries, Journal of

Electroanalytical Chemistry, 794 (2017) 120-125.

[48] H. Yang, X.-H. Wang, Y.-X. Qi, N. Lun, Y.-M. Cao, Y.-J. Bai, Improving the electrochemical performance of $Li_2ZnTi_3O_8$ by surface KCl modification, ACS Sustainable Chemistry & Engineering, 5 (2017) 6099-6106.

[49] H. Yang, N. Lun, Y.-X. Qi, H.-L. Zhu, J.-R. Liu, J.-K. Feng, L.-l. Zhao, Y.-J. Bai, $Li_2ZnTi_3O_8$ coated with uniform lithium magnesium silicate layer revealing enhanced rate capability as anode material for Li-ion battery, Electrochimica Acta, 315 (2019) 24-32.

[50] J.-L. Qin, H.-L. Zhu, N. Lun, Y.-X. Qi, Y.-J. Bai, $Li_2ZnTi_3O_8$/C anode with high initial Coulombic efficiency, long cyclic life and outstanding rate properties enabled by fulvic acid, Carbon, 163 (2020) 297-307.

[51] H. Yang, J. Park, C.-S. Kim, Y.-H. Xu, H.-L. Zhu, Y.-X. Qi, L.-W. Yin, H. Li, N. Lun, Y.-J. Bai, Boosted electrochemical performance of $Li_2ZnTi_3O_8$ enabled by ion-conductive $Li_2ZrO_3$ concomitant with superficial Zr-doping, Journal of Power Sources, 379 (2018) 270-277.

[52] H. Yang, H.-L. Zhu, Y.-X. Qi, N. Lun, Y.-J. Bai, Optimizing the cycling life and high-rate performance of $Li_2ZnTi_3O_8$ by forming thin uniform carbon coating derived from citric acid, Journal of Materials Science, 55 (2020) 15538-15550.

[53] X. Zeng, J. Peng, H. Zhu, Y. Gong, X. Huang, Cr-doped $Li_2ZnTi_3O_8$ as a high performance anode material for lithium-ion batteries, Frontiers in Chemistry, 8 (2020) 600204-600210.

[54] H. Tang, T. Liu, Z. Tang, The stereo-microstructure of ZnO affects the lithium

storage capacity of $Li_2ZnTi_3O_8$ anode materials, Dalton Transactions, 48 (2019) 12303-12314.

[55] H. Tang, Y. Song, L. Zan, Y. Yue, D. Dou, Y. Song, M. Wang, X. Liu, T. Liu, Z. Tang, Characterization of lithium zinc titanate doped with metal ions as anode materials for lithium ion batteries, Dalton Transactions, 50 (2021) 3356-3368.

[56] Y. Li, T.-F. Yi, X. Li, X. Lai, J. Pan, P. Cui, Y.-R. Zhu, Y. Xie, $Li_2ZnTi_3O_8$@α-$Fe_2O_3$ composite anode material for Li-ion batteries, Ceramics International, 47 (2021) 18732-18742.

[57] L. Qiu, X.-Q. Lai, F. Wang, J. Pan, Y.-R. Zhu, P. Cui, T.-F. Yi, Promoting the Li storage performances of $Li_2ZnTi_3O_8$@$Na_2WO_4$ composite anode for Li-ion battery, Ceramics International, 47 (2021) 19455-19463.

[58] T.-F. Yi, J.-Z. Wu, J. Yuan, Y.-R. Zhu, P.-F. Wang, Rapid lithiation and delithiation property of V-doped $Li_2ZnTi_3O_8$ as anode material for lithium-ion battery, ACS Sustainable Chemistry & Engineering, 3 (2015) 3062-3069.

[59] Y. Yuan, F. Chen, G. Cai, S. Yin, M. Zhu, L. Wang, J. Yang, S. Guo, Ultrafine $TiO_2$ nanocrystalline anchored on nitrogen-doped amorphous mesoporous hollow carbon nanospheres as advanced anode for lithium ion batteries, Electrochimica Acta, 296 (2019) 669-675.

[60] Y. Wang, N. Li, C. Hou, B. He, J. Li, F. Dang, J. Wang, Y. Fan, Nanowires embedded porous $TiO_2$@C nanocomposite anodes for enhanced stable lithium and sodium ion battery performance, Ceramics International, 46 (2020) 9119-9128.

[61] X. Shen, M. Chen, X. Hong, W. Wang, Z. Qiao, J. Chen, S. Fan, J. Yu, C. Tang,

Synthesis and anodic performance of $TiO_2$-carbonized PAN electrode for lithium ion batteries, Chemical Physics, 530 (2020) 110639-110643.

[62] X. Zhao, H. Liu, M. Ding, Y. Feng, In-situ constructing of hollow $TiO_2$@rGO hybrid spheres as high-rate and long-life anode materials for lithium-ion batteries, Ceramics International, 45 (2019) 12476-12483.

[63] S.-I. Oh, J.-C. Kim, M.A. Dar, D.-W. Kim, Synthesis and characterization of uniform hollow $TiO_2$ nanofibers using electrospun fibrous cellulosic templates for lithium-ion battery electrodes, Journal of Alloys and Compounds, 800 (2019) 483-489.

[64] A.A. Kashale, A.S. Rasal, G.P. Kamble, V.H. Ingole, P.K. Dwivedi, S.J. Rajoba, L.D. Jadhav, Y.-C. Ling, J.-Y. Chang, A.V. Ghule, Biosynthesized Co-doped $TiO_2$ nanoparticles based anode for lithium-ion battery application and investigating the influence of dopant concentrations on its performance, Composites Part B: Engineering, 167 (2019) 44-50.

[65] W. Song, Q. Jiang, X. Xie, A. Brookfield, E.J.L. McInnes, P.R. Shearing, D.J.L. Brett, F. Xie, D.J. Riley, Synergistic storage of lithium ions in defective anatase/rutile $TiO_2$ for high-rate batteries, Energy Storage Materials, 22 (2019) 441-449.

[66] Y. Liu, M. Guo, Z. Liu, Q. Wei, M. Wei, Rapid and facile synthesis of hierarchically mesoporous $TiO_2$–B with enhanced reversible capacity and rate capability, Journal of Materials Chemistry A, 6 (2018) 1196-1200.

[67] J.-F. Wang, J.-J. Zhang, D.-N. He, Flower-like $TiO_2$-B particles wrapped by graphene with different contents as an anode material for lithium-ion batteries, Nano-

Structures & Nano-Objects, 15 (2018) 216-223.

[68] J.-Y. Liao, B.D. Luna, A. Manthiram, $TiO_2$-B nanowire arrays coated with layered $MoS_2$ nanosheets for lithium and sodium storage, Journal of Materials Chemistry A, 4 (2016) 801-806.

[69] M. Cao, L. Gao, X. Lv, Y. Shen, $TiO_2$-B@$VS_2$ heterogeneous nanowire arrays as superior anodes for lithium-ion batteries, Journal of Power Sources, 350 (2017) 87-93.

[70] Y. Yuan, H. Yu, X. Cheng, R. Zheng, T. Liu, N. Peng, N. Long, M. Shui, J. Shu, Preparation of $TiNb_6O_{17}$ nanospheres as high-performance anode candidates for lithium-ion storage, Chemical Engineering Journal, 374 (2019) 937-946.

[71] Q. Fu, J. Hou, R. Lu, C. Lin, Y. Ma, J. Li, Y. Chen, Electrospun $Ti_2Nb_{10}O_{29}$ hollow nanofibers as high-performance anode materials for lithium-ion batteries, Materials Letters, 214 (2018) 60-63.

[72] W. Mao, K. Liu, G. Guo, G. Liu, K. Bao, J. Guo, M. Hu, W. Wang, B. Li, K. Zhang, Y. Qian, Preparation and electrochemical performance of $Ti_2Nb_{10}O_{29}$/Ag composite as anode materials for lithium ion batteries, Electrochimica Acta, 253 (2017) 396-402.

[73] Y. Zhang, M. Zhang, Y. Liu, H. Zhu, L. Wang, Y. Liu, M. Xue, B. Li, X. Tao, Oxygen vacancy regulated $TiNb_2O_7$ compound with enhanced electrochemical performance used as anode material in Li-ion batteries, Electrochimica Acta, 330 (2020) 135299-135308.

[74] J. Luo, J. Peng, P. Zeng, Z. Wu, J. Li, W. Li, Y. Huang, B. Chang, X. Wang, $TiNb_2O_7$ nano-particle decorated carbon cloth as flexible self-support anode material

in lithium-ion batteries, Electrochimica Acta, 332 (2020) 135469-135479.

[75] S. Yoon, S.-Y. Lee, T.L. Nguyen, I.T. Kim, S.-G. Woo, K.Y. Cho, Controlled synthesis of dual-phase carbon-coated $Nb_2O_5/TiNb_2O_7$ porous spheres and their Li-ion storage properties, Journal of Alloys and Compounds, 731 (2018) 437-443.

[76] S. Lou, X. Cheng, J. Gao, Q. Li, L. Wang, Y. Cao, Y. Ma, P. Zuo, Y. Gao, C. Du, H. Huo, G. Yin, Pseudocapacitive $Li^+$ intercalation in porous $Ti_2Nb_{10}O_{29}$ nanospheres enables ultra-fast lithium storage, Energy Storage Materials, 11 (2018) 57-66.

[77] J. Gao, X. Cheng, S. Lou, Y. Ma, P. Zuo, C. Du, Y. Gao, G. Yin, Self-doping $Ti_{1-x}Nb_{2+x}O_7$ anode material for lithium-ion battery and its electrochemical performance, Journal of Alloys and Compounds, 728 (2017) 534-540.

[78] W. Liu, X. Zhang, C. Li, K. Wang, X. Sun, Y. Ma, Carbon-coated $Li_3VO_4$ with optimized structure as high capacity anode material for lithium-ion capacitors, Chinese Chemical Letters, 31 (2020) 2225-2229.

[79] N. Gautam, R. Muhammad, H. Raj, A. Sil, P. Mohanty, T.K. Mandal, Multimodal mesopore hierarchy in $Li_3VO_4$ boosts electrochemical anode performance of lithium-ion batteries, Microporous and Mesoporous Materials, 290 (2019) 109669-109673.

[80] R. Qin, G. Shao, J. Hou, Z. Zheng, T. Zhai, H. Li, One-pot synthesis of $Li_3VO_4$@C nanofibers by electrospinning with enhanced electrochemical performance for lithium-ion batteries, Science Bulletin, 62 (2017) 1081-1088.